ELSEVIER

Contents lists available at ScienceDirect

# **Applied Materials Today**

journal homepage: www.elsevier.com/locate/apmt



# Recovering magnetic domains of nanoscale-mechanically damaged ferromagnetic thin film of information data storage

Chang-Dong Yeo<sup>a,\*</sup>, Muyang He<sup>a,d</sup>, Jaeho Lee<sup>a</sup>, Nayem Mohammed Reza Shah<sup>a</sup>, Yang-Ki Hong<sup>b,\*</sup>, Minyeong Choi<sup>b</sup>, Jeong Ho You<sup>c</sup>, Dipesh Purani<sup>e</sup>, Jung Kyu Lee<sup>f</sup>

- <sup>a</sup> Department of Mechanical Engineering, Texas Tech University, Lubbock, TX 79409, USA
- b Department of Electrical and Computer Engineering and Materials Science Ph.D. Program, The University of Alabama, Tuscaloosa, Alabama 35487, USA
- <sup>c</sup> School of Engineering, University of St. Thomas, St. Paul, Minnesota 55105, USA
- <sup>d</sup> School of Mechanical Engineering, Guizhou University, Guiyang, Guizhou Province, China
- e Head Disk Interface Group, Seagate Technology, Shakopee, Minnesota 55379, USA
- <sup>f</sup> Hysitron Nanomechanical Test Instruments, Bruker, Eden Prairie, Minnesota 55344, USA

#### ARTICLE INFO

#### Article history: Received 27 July 2020 Revised 3 September 2020 Accepted 5 September 2020

Keywords: Ferromagnetic film Magnetic recovery Nanoscratch Scratch deepening Phase change

#### ABSTRACT

Combined effects of stress and temperature on magnetic domains and scratch morphology of the ferromagnetic film of a perpendicular magnetic recording media are investigated using nanoscratch, atomic force microscope, and magnetic force microscope. The stored magnetic signals in the non-scratched area become weak with increasing temperature due to the thermal agitation of magnetic spins. The high local stress permanently damages the magnetic signals at the scratch center. However, the weakened magnetic signals at lightly stressed regimes recover significantly with increasing temperature up to 300 °C due to the partial recovery of ferromagnetism. Regarding the nanoscratch morphology, when the temperature increases up to 300 °C, the scratch is healed noticeably due to metal oxides (CoO, Cr<sub>2</sub>O<sub>3</sub>, and PtO<sub>2</sub>) built-up on the scratched surface. Surprisingly, the scratch deepens at 400 - 600 °C. This is attributed to PtO<sub>2</sub> evaporation and the phase transition of magnetic grains from HCP to FCC.

© 2020 Elsevier Ltd. All rights reserved.

# 1. Introduction

By 2025, the billions of Internet of Things (IoT) devices will be connected across the globe. More than 90 ZB (1 Zettabyte =  $10^{21}$  bytes) of information data will be created within five years [1]. Furthermore, the novel Coronavirus-19 surge has been rapidly changing human societal infrastructure and wild nature, i.e., environment. Our community infrastructure takes online digital communication, thereby requiring substantial information data storage systems. In response to this, commercial sector companies are diligently changing their marketing strategy to wirelessly connected and digitized infrastructure, i.e., information technology (IT). Accordingly, the annual data created worldwide is skyrocketing; thus, super high-density hard disk drive (HDD) is demanded ever to store digital information. An HDD is composed of magnetic recording media, writing and reading heads, actuators, and accessory components.

Recording media (made of magnetic thin films) needs to be thermally stable, capable of writing information with a low mag-

E-mail addresses: changdong.yeo@ttu.edu (C.-D. Yeo), ykhong@eng.ua.edu (Y.-K. Iong).

netic field, and high signal-to-noise ratio (SNR). The thermal stability is determined by  $K_{\rm u}V/k_{\rm B}T$ , where  $K_{\rm u}$  is the magnetocrystalline anisotropy constant, V is the volume of magnetic grain,  $k_{\rm B}$  is the Boltzmann constant, and T is the temperature. Media reliability requires  $K_{\rm u}V/k_{\rm B}T>60$  for 2–4 nm magnetic grains [2,3]; therefore, spontaneous reversal via thermal agitation (i.e., superparamagnetism) is not allowed to set in. Magnetic grain becomes unstable as the grain size decreases, but the SNR increases. This means that the thermal stability refutes SNR. The SNR also increases with decreasing head-to-media interface (HDI) spacing. Therefore, future recording media requires 4 nm-sized grain and extremely narrow HDI spacing of less than 1.5 nm [4,5]. The latter can create a tribological issue caused by HDI contact.

Current HDD uses the perpendicular recording technology based on perpendicular magnetic recording (PMR) media, i.e., a thin film of CoCrPt-SiO<sub>2</sub> [6–8]. Its areal storage density (AD) is approaching 1.5 Tb/in<sup>2</sup> with the shingled magnetic recording (SMR) design. The magnetic grain size of the media is 7 - 10 nm, and the grains are perpendicularly magnetized, where the magnetic spin direction is out-of-plane. The grains are segregated from each other by the SiO<sub>2</sub> layer precipitated to the grain boundary. The schematic of the media structure is presented in Fig. S1 (Supplementary Material) to help readers understand the structure of magnetic

<sup>\*</sup> Corresponding authors.

recording media, where information is stored. The data capacity of PMR-based HDD could not keep up with demanded digital information data size due to the low magnetocrystalline anisotropy energy (i.e., coercivity), the thermal instability of magnetic grain, and the saturation of writing head. PMR media quality relies on the degree of decoupling magnetic grains by low surface energy oxides, which can significantly increase the surface roughness [9]. The rough surface of magnetic thin film media can result in the tribological problems for HDI [10–12].

Heat-assisted magnetic recording (HAMR) [13–16] and microwave-assisted magnetization reversal (MAMR) [17] technologies have been proposed to push the present AD of about 1.5 Tb/in<sup>2</sup> to be higher. The information data storage industry strives to achieve 32 TB (terabytes) HDD using HAMR or MAMR technology. The recording media is based on  $L_{10}$  FePt, which has much higher magnetocrystalline anisotropy energy than that of CoCrPt used in PMR. Therefore, the thermal instability of FePt grain is not an issue, but a large magnetocrystalline anisotropy of the FePt potentially saturates the writing head. HAMR uses a highpowered laser source to heat a small local area of the recording media during the writing process [18,19]. The temperature of the heated spot in media goes up to 400 - 500 °C. Accordingly, the media coercivity can be temporarily lowered below the magnetic write field, which enables high magnetocrystalline anisotropy and nano-sized grains to be thermally stable. We have studied Fe-Mn-Pt for HAMR to reduce its magnetocrystalline anisotropy energy [20,21]. It was found that alloying Fe-Pt with Mn lowered magnetocrystalline anisotropy energy while maintaining acceptable magnetization and  $T_c$  for the HAMR application. The resulting data meet 100 emu/cm $^3$  of saturation magnetization ( $M_s$ ), 100 kOe of magnetocrystalline anisotropy field ( $H_k$ ), 600 K - 650 K of  $T_c$ , required to achieve the data storage capacity of 4 Tb/in<sup>2</sup> [4].

In HDD industry, the magnetic grain size needs to be smaller than 5 nm, and the HDI spacing approaches 1.1 nm to achieve the areal recording density of 4 Tb/in<sup>2</sup> [3,5]. Reduction in both magnetic grain size and HDI spacing creates two issues. One is the superparamagnetic behavior of magnetic grain (i.e., demagnetization), and the other is the possibility of scratching damage on magnetic recording media during HDI interactions. Mechanical stress incurred by HDI contact changes magnetocrystalline anisotropy energy, which accordingly can change the magnetization and permeability of magnetic thin film [22-24]. Magnetostriction also sets in PMR thin film during magnetization reversal with the applied magnetic field. The saturation magnetostriction of  $(Co_{72}Cr_{18})_{79}Pt_{21}/1100$  Å Ti bilayer was measured to be about  $8 \times 10^{-5}$  [25]. The existence of magnetostriction implies that applied mechanical stress can alter the domain structure by changing the magnetocrystalline anisotropy [26]. Therefore, the magnetostriction is one of the subject issues in recording media design, but out of this study.

In this paper, we report the magnetic and morphological response of the magnetic layer (Co-Cr-Pt) of PMR media to the mechanical contact stress and heat. Physical phenomena and stress/heat-induced magnetism changes in the scratched and surrounding areas are quantified and explained. The outcomes of this study will provide the fundamental design rules for HAMR-based HDD to secure its long-term reliability.

### 2. Material and methods

### 2.1. 2T magnetic pattern written on PMR media

A PMR media was prepared by Seagate Technology (Minnesota, USA). Fig. 1a shows a cross-sectional high-resolution transmission electron microscope (HRTEM) image for PMR media. The media is a layered structure, containing a surface protective diamond-like

carbon (DLC) film, a magnetic layer (made of CoCrPt and additives), interlayers, a soft magnetic underlayer, and a substrate. The epitaxial growth of the magnetic layer forms a column-like structure (HCP structure of CoCrPt), enabling efficient magnetic exchange in a vertical direction. In this research, 2T magnetic patterns ('T' is the fundamental bit interval) were written on the PMR media so that a change in magnetic signals with combined mechanical stress and temperature is measured quantitatively. Fig. 1b shows the magnetic force microscopy (MFM) image and magnetic phase angle data of 2T patterns. The array of black and white spots (similar to a chessboard) is the magnetic domains with upward and downward magnetizations, which generate a sine wave curve of the magnetic phase angle with a uniform amplitude. The rectangular magnetic domain size is 80 nm  $\times$  100 nm, and their magnetic strength is evaluated using the peak-to-peak amplitude of magnetic phase angles.

### 2.2. Nanoscratch experiment

Fig. S2 (Supplementary Material) shows the schematics of nanoscratch process including load-displacement profiles. A lithography AFM probe (i.e., HQ:NSC16/Hard/AI BS made by MikroMasch® with the tip radius smaller than 8 nm) that is coated with a layer of hardened DLC was used in this experiment. Using the lithography function of Asylum Research® MFP-3D AFM, the probe was positioned on the 2T patterned area, and then constant-load (Figs. S2b and S2c, Supplementary Material) and ramp-load (Figs. S2d and S2e, Supplementary Material) nanoscratch were performed. First, the constant-load nanoscratch experiments were conducted under three different normal forces (10.6 mN, 17.7 mN, and 31.9 mN) to examine the relationship between mechanical stress and magnetic property change. Next, the ramp-load nanoscratch experiment was carried out by increasing the normal contact load linearly from 0 mN to 31.9 mN. The tip sliding velocity and the sliding distance (or scratch length) were 1  $\mu$ m/s and 5  $\mu$ m, respectively, for both constant- and ramp-load nanoscratch experiments. Fig. S3 (Supplementary Material) shows the AFM and MFM images of the four nanoscratches produced by three constant-load and one ramp-load profiles. It was ascertained that the probe tip was exactly located within the 2T magnetic patterned area, and the results showed that the higher normal forces produced the deeper and wider scratches with more magnetic damage. Since the rootmean-square (RMS) roughness of the PMR media was 0.22 nm (i.e., a mirror-like smooth surface) and the monolayer thick PFPE lubricant on the surface is much softer than the underlying DLC and magnetic layers, its effect on the nanoscratch experiment was deemed negligible.

### 2.3. Heat processing to PMR media

After finishing the nanoscratch experiments at room temperature, we investigated the effect of temperature on the change in physical morphology and magnetic properties near the scratch regime (i.e., mechanically stressed area). This experiment enabled us to investigate the individual and coupled effects of stress and temperature on the mechanical and magnetic behavior of ferromagnetic materials. The sample was heated up to 600 °C (i.e., heating to 100 °C, 200 °C, 300 °C, 400 °C, 500 °C, and 600 °C). Upon reaching the elevated target temperature with the duration time of 10 min, the sample was cooled down to room temperature. Afterwards, AFM and MFM measurements were carried out at the same location of nanoscratch. The mechanical degradation was evaluated using the topography data of AFM measurement, while the magnetic degradation was analyzed using the phase angle signal of MFM measurement.

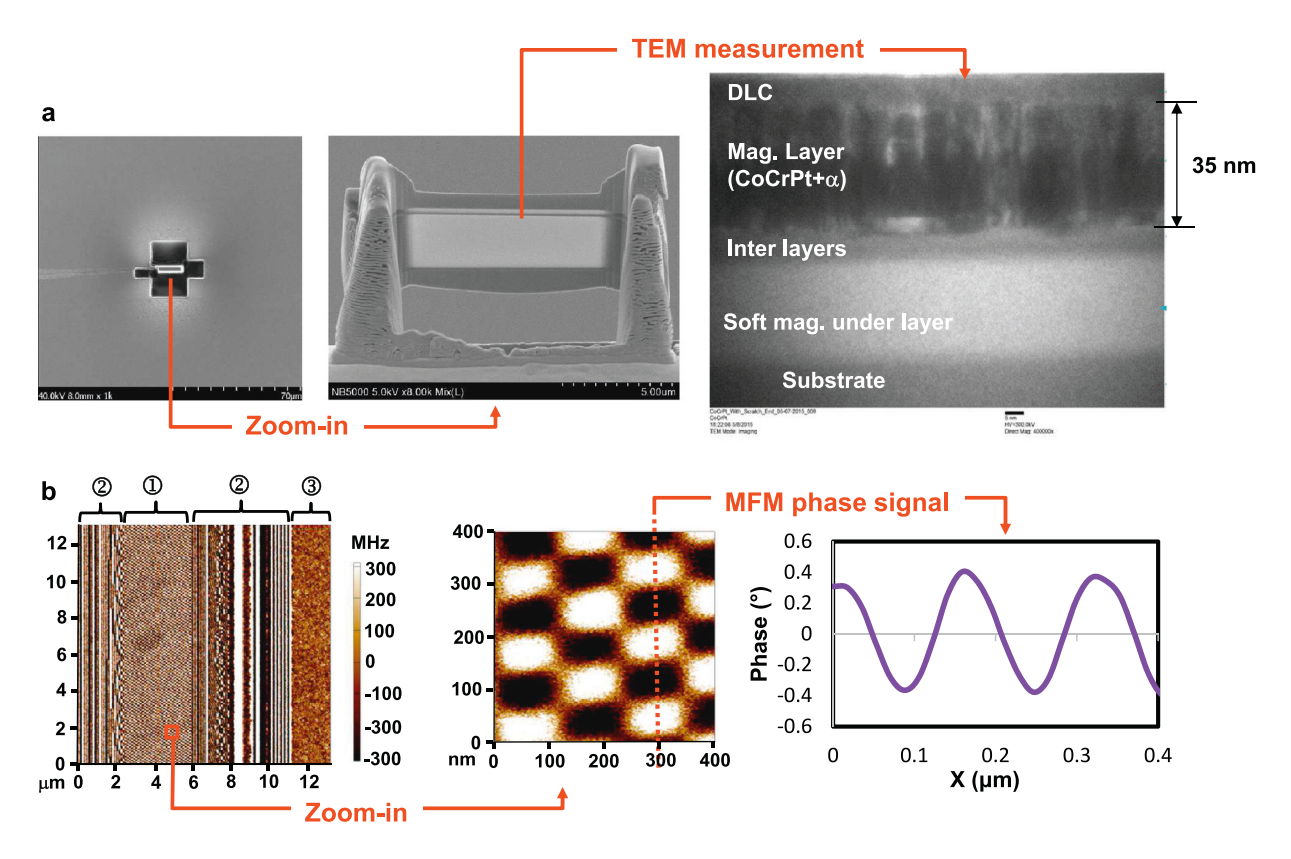


Fig. 1. PMR media written with 2T magnetic patterns. a Focused ion beam (FIB) to prepare a thin vertical film for TEM measurement. The measured TEM image provides the layered structure of PMR media composed of DLC coating, magnetic layers, and substrate. b MFM image of PMR media showing 2T magnetic patterns with repeated upward (white rectangular spot) and downward (black rectangular spot) arrays of magnetic spins. ①–2T patterns, ②–DC servo patterns, and ③-Non-magnetized area. The magnetic phase angle across the 2T patterned area (red-dotted line) have a sinewave form with uniform amplitude.

# 2.4. Nanoindentation experiment

The mechanical properties (i.e., hardness and reduced elastic modulus) of PMR media were measured through the nanoindentation technique. With the nanoindentation system of Hystron TI 980 by Bruker® and xProbe (= indenter), the standard quasi-static trapezoid load function was used for the quasi static tests. Fig. S4a (Supplementary Material) shows a standard quasi-static trapezoid load function that was used for the quasi static tests. To measure and analyze the mechanical properties of magnetic layer in Fig. 1a, the peak load gradually increased to 350  $\mu$ N so that the contact depth could reach up to 40 nm. Figs. S4b and S4c (Supplementary Material) show the actual load-displacement curves used in nanoindentation experiment for unheated and 600 °C heated PMR media samples, respectively. Based on the method developed by Oliver and Pharr [27,28], hardness of the PMR media could be obtained as a function of contact depth.

### 3. Results

# 3.1. Numerical simulation co calculate contact stress during nanoscratch experiment

Contact stress causes a PMR media to experience its mechanical (i.e., permanent deformation and wear) and magnetic (i.e., the agitation of magnetic spins) damage. Numerical simulation of a sliding contact was conducted to estimate the contact stress during the nanoscratch experiment. The input material properties and geometric parameters are based on the nanoscratch tip and the PMR media in experiment. The detailed procedures are described in Appendix. Fig. 2 shows the schematic of the sliding contact model

and the resulting von Mises stress around the contact area on PMR media caused by the nanoscratch tip. Under the constant load of P = 31.9 mN, the contact stress is high enough to initiate the plastic deformation, thereby producing physical scratches on the PMR media surface. From the stress contour in Fig. 2b, the maximum von Mises stress (= 415 GPa) occurs at the trailing edge of the circular contact spot. This suggests that the high contact stress at the trailing edge can generate a deep scratch valley (i.e., (1) in the inlet of Fig. 2b). Outside of the scratch wedge (i.e., locations (2) and (3) in Fig. 2b), the von Mises stress is relatively low, i.e., 90 GPa. The high stress around the contact zone can cause the magnetic grains to be deformed and tilted along the sliding direction, which results in demagnetization of the magnetic domains [29]. It is noted that the actual scratch width after the nanoscratch experiment is smaller than the contact spot size in Fig. 2b because of the elastic recovery during tip unloading.

### 3.2. Critical loads for mechanical and magnetic degradation

During the nanoscratch experiments, the magnetic properties of PMR media are changed by mechanical contact stress. The critical stress to initiate magnetic degradation is not the same as the mechanical yield stress but depends on the ferromagnetic film's design parameters. Fig. 3 shows the ramp-load nanoscratch experiment results, indicating the mechanical and magnetic degradation of PMR media. The nanoscratch is 5  $\mu$ m long, and the normal load linearly increases from 0 mN (at  $x=0.0~\mu$ m) to 31.9 mN (at  $x=5.0~\mu$ m) in this experiment. As shown in the atomic force microscope (AFM) image of Fig. 3a and the surface topography (a blue-solid line) of Fig. 3b, the media surface did not show any scratch marks at the early stage of sliding contact, indicating

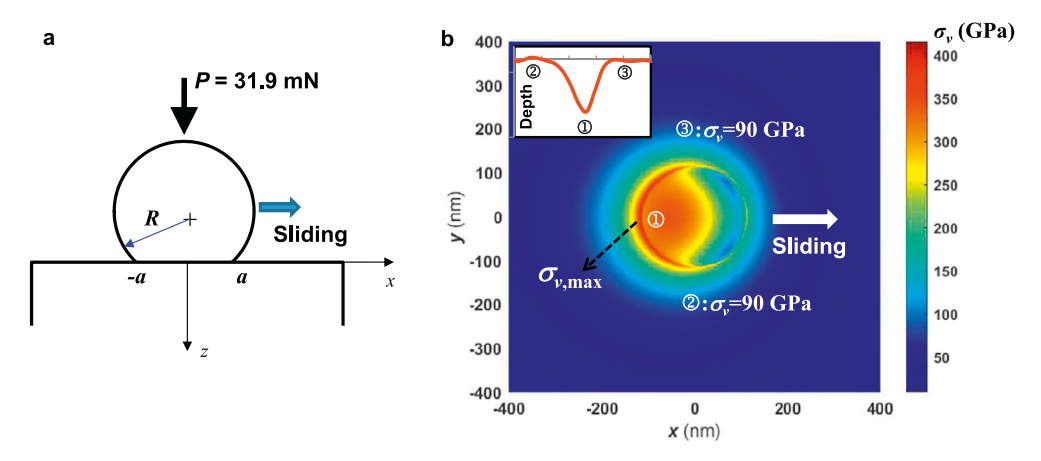


**Fig. 2.** Calculation of mechanical contact stress during nanoscratch experiment. **a** Schematic (side view) of the sliding contact between a spherical tip and media surface (R=radius of scratch tip, P=contact load, a=semi-contact width). The nanoscratch tip was assumed to be hemispherical with the radius of 30 nm. **b** The resulting von Mises stress distribution around contact area under the normal contact load of 31.9 mN (top view). The inlet is the actual scratch profile from the constant load nanoscratch with 31.9 mN, where ( $\hat{I}$ ) is the scratch center having the maximum stress of 415 GPa and ( $\hat{I}$ )&( $\hat{I}$ ) are outside of the scratch wedge with relatively lower stress of 90 GPa.

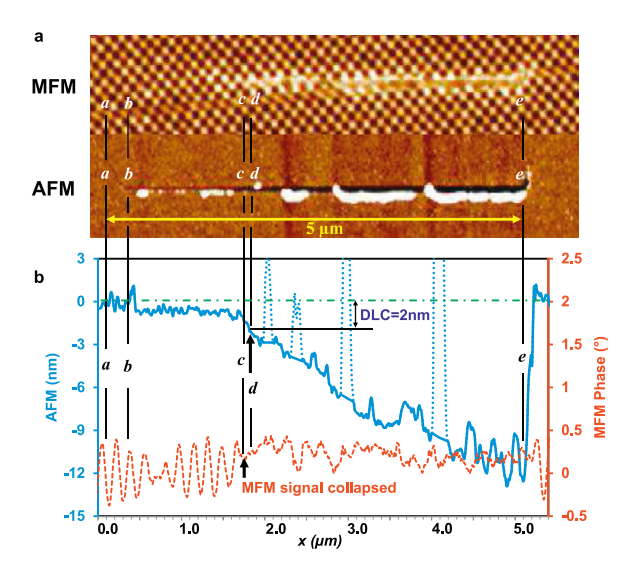


**Fig. 3.** AFM and MFM measurements after the ramp-load nanoscratch experiment. **a** MFM and AFM images on the scratched area (top view). **b** Surface profiles from MFM and AFM data, which were measured along the scratch center line. The points of a and e are the start and finish of the scratch, respectively. The plastic deformation of DLC film initiates at b, the damage of magnetic signal initiates at c, and the DLC film is completely removed at d.

the regime a - b is an elastic contact. Permanent deformation initiated at the sliding distance of  $x = 0.25 \mu m$  (point b, normal contact load = 1.6 mN). Then, the scratch depth gradually deepened until the DLC film (thickness = 2 nm) was completely removed at  $x = 1.74 \ \mu \text{m}$  (point d, normal contact load = 11.1 mN). Beyond the point d, the scratch depth steeply deepened because the underlying magnetic layer is softer than the DLC film. It is noted that the blue-dashed line in Fig. 3b represents wear particles (whitecolored along with the scratch in the AFM image of Fig. 3a) located in the middle of wear track. The MFM image of Fig. 3a and the magnetic phase profile (a red-dashed line) of Fig. 3b reveal that the magnetic signal (i.e., the baseline and amplitude of the MFM phase angle) did not change significantly at the beginning of the ramp-load scratch. However, it was abnormally deteriorated beyond the sliding distance of  $\sim$  1.65  $\mu$ m (point c, normal contact load = 10.5 mN). At point c, the scratch depth is ~ 1.0 nm, indicating that the DLC film still covers the underlying magnetic layer. Afterward, the magnetic signal became significantly weakened at the contact regime c-e due to the high contact stress. By comparing the AFM to MFM results, we realize that although the DLC film developed permanent deformation and wear in the beginning of sliding contact (regime a-c), the magnetic signal was not affected much. This observation supports that the DLC film functioned to protect the PMR media from magnetic degradation. It was also observed that the initiation of magnetic degradation (point c, normal contact load c 10.5 mN) occurred before the DLC film was removed entirely (point c, normal contact load c 11.1 mN). This is attributed to the high local stress beneath the nanoscratch tip, which was high enough to distort the underlying magnetic grains' crystalline structure.

# 3.3. Quantitative comparison of mechanical and magnetic degradation of PMR

The constant-load nanoscratch experiment was performed with three different loads of 10.6 mN, 17.7 mN, and 31.9 mN to investigate the consequent relationship between mechanical and magnetic degradations of PMR media. After the nanoscratch on the PMR media surface, the scratch widths measured from AFM and MFM data were used to evaluate the mechanical and magnetic degradations. Fig. 4 describes the schemes to quantify the physical and magnetic scratch widths using the 31.9 mN constantload nanoscratch results. The scratch profile and magnetic signal in Fig. 4c and d were obtained along the red-line in the AFM and MFM images of Fig. 4a and b, respectively. The nanoscratch experiment has generated pile-ups on both sides of the scratch track due to material displacements and wear particles (white-colored line along with the scratch in Fig. 4a). The physical scratch width was calculated from the AFM data as depicted in Fig. 4c; the width based on the center-line-average (CLA),  $w_1$ , and the peak-to-peak width,  $w_2$ . The scratch depth, d, was measured by the vertical distance from the CLA line to the scratch valley. In Fig. 4a and c, the pile-up on the right side of the scratch track was taller than that on the left side. This is attributed to the tilted tip engagement angle. During the nanoscratch experiment, the scratch tip was slanted to the right, which caused the right face of the tip to develop higher contact stress, thereby leading to more pile-up and wear debris on the right wedge area. The scratch width from MFM data,  $w_{\rm m}$ , was measured by the width of collapsed sign wave signal, as depicted in Fig. 4d. The collapse of the pseudo sign wave indicates the degradation of the magnetic signal or disturbance of magnetic spins. The scratch widths and depth are summarized in Table 1. It

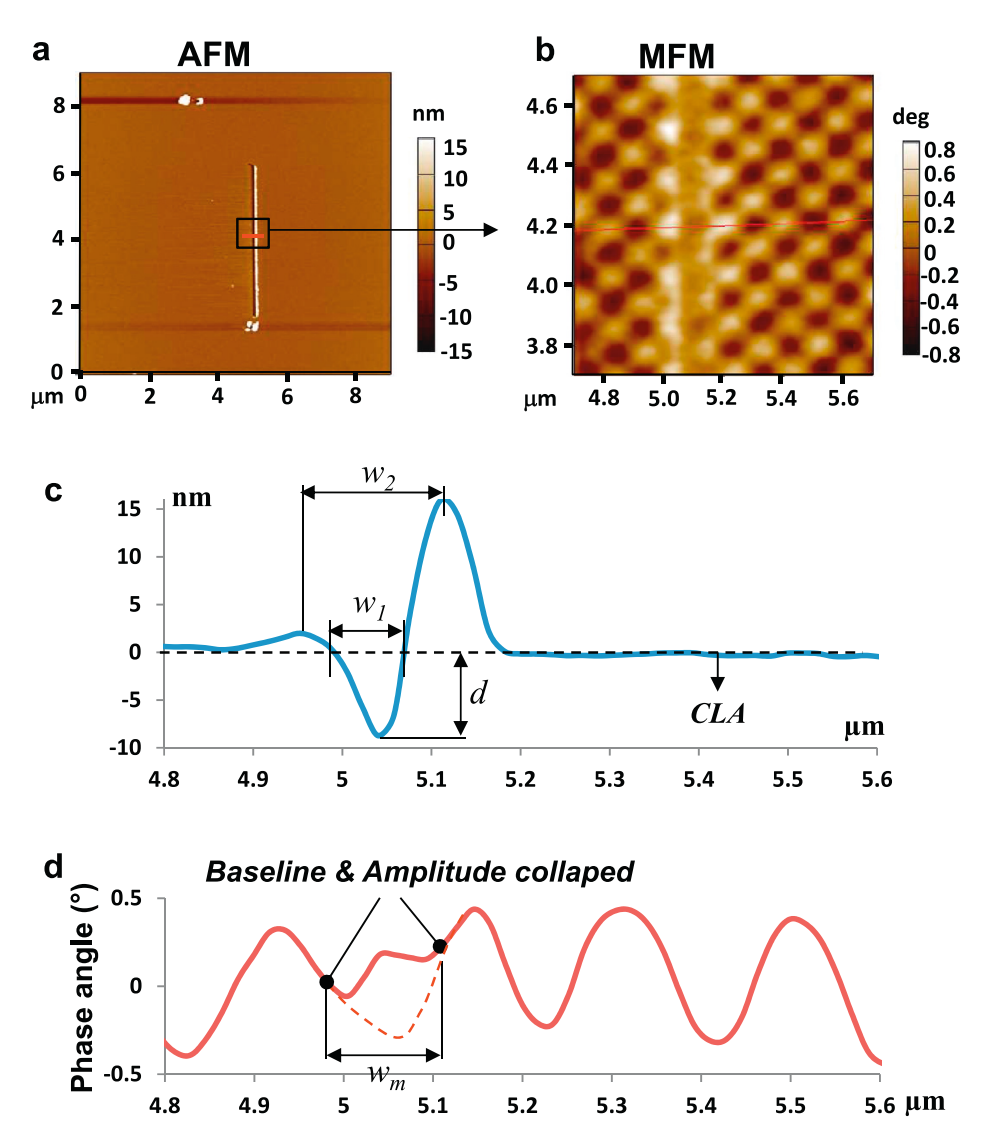


**Fig. 4.** Quantification of the scratch width based on AFM and MFM data. The schemes were explained using the results of the 31.9 mN constant-load nanoscratch. **a** AFM image including the  $5\mu$ m scratch. **b** The zoomed-in MFM image of the black square area to show the magnetic patterns clearly. **c** Using the AFM scratch profile along the red line in **a**, the physical scratch width was measured by the center-line-average (CLA), i.e.,  $w_1$ , and the peak-to-peak distance between the piled-up wedges, i.e.,  $w_2$ . The scratch depth (d) was calculated by the vertical distance from the CLA to the scratch valley. **d** Using the MFM scratch profile along the red line in **b**, the magnetic scratch width, i.e.,  $w_m$ , was determined by the interval, in which the baseline and amplitude of the magnetic signal was disrupted. The red-dashed line is the expected non-damaged magnetic signal.

**Table. 1**Quantitative comparison of mechanical and magnetic degradation at room temperature. The magnitude of mechanical and magnetic degradation was measured by the scratch width from AFM and MFM data, respectively.

	31.9 mN	17.7 mN	10.6 mN
$w_1$ $w_2$ $d$ $w_m$	106.7 ± 37.4 nm	$106.2 \pm 11.7 \text{ nm}$	$55.1 \pm 18.0 \text{ nm}$
	176.2 ± 30.5 nm	$149.5 \pm 13.4 \text{ nm}$	$86.6 \pm 27.2 \text{ nm}$
	7.9 ± 2.0 nm	$4.5 \pm 1.1 \text{ nm}$	$1.2 \pm 0.3 \text{ nm}$
	152.7 ± 36.7 nm	$121.7 \pm 24.4 \text{ nm}$	No damage

is noted that, for the constant load of 10.6 mN, the scratch depth (d=1.2 nm) was smaller than the DLC thickness (=2.0 nm), and the contact stress was not high enough to degrade the underlying magnetic domains significantly. Therefore, the  $w_m$  value is meaningless for such a low load of 10.6 mN. The results of 17.7 mN and 31.9 mN contact loads found that the  $w_m$  is larger than  $w_1$  but smaller than  $w_2$ . As schematically described in Fig. 5, during the nanoscratch experiment, magnetic grains near the scratch center are physically distorted by the high contact stress. This distortion

can decrease the magnetocrystalline anisotropy energy, thereby changing the magnetic spins' direction or weakening the magnetic signals [30–32]. Therefore, it is suggested that the magnetic domains within the scratch track are damaged significantly, disturbing their spin directions. In contrast, the effect of contact stress on the magnetic domains outside the scratch track is not significant; therefore, their original magnetic spin directions are mostly retained, indicating a limited reduction of magnetic phase angle amplitude, as seen in Fig. 4d.

# 3.4. Combined effect of stress and temperature on magnetic properties

The scratched (i.e., stressed) and non-scratched (i.e., unstressed) areas respond differently to temperature for magnetic properties. The nanoscratched sample with a constant load of 31.9 mN was analyzed with increasing temperature to investigate the combined effects of stress and temperature on magnetic properties. Fig. 6a–f provide the MFM images, showing the 5  $\mu$ m long scratch and 2T magnetic patterns. The magnetic domains in the non-scratched

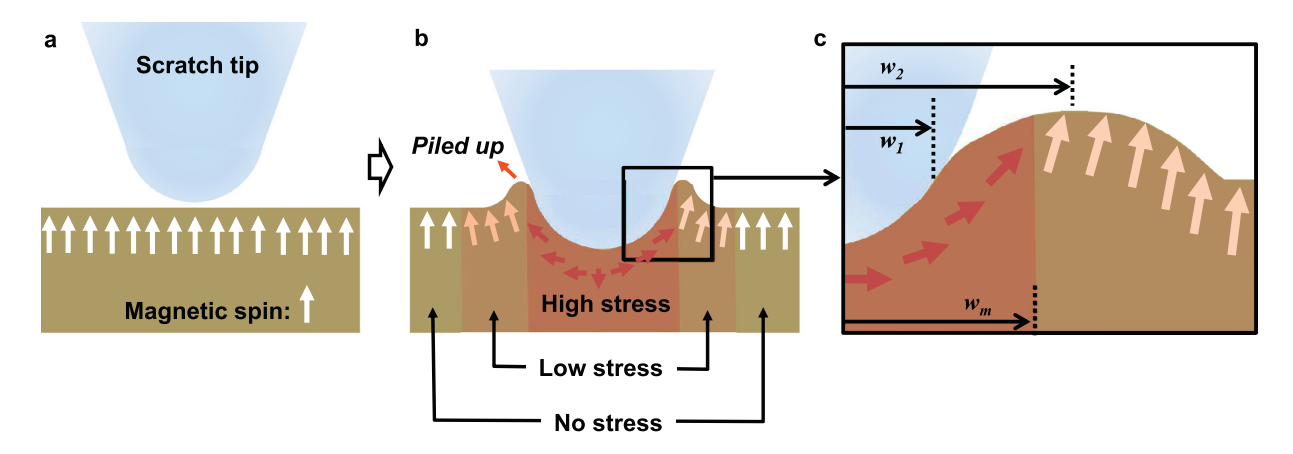


**Fig. 5.** Schematic of magnetic degradation near the contact region during nanoscratch experiment. **a** Initial magnetic spins before the scratch contact. All magnetic spins are directed upward with the same magnetic strength. **b** During the nanoscratch, magnetic spins near the scratch center are shrinking or rotated significantly by the high contact stress. **c** Compared to the inner side of the wedge, the outer side develops relatively lower contact stress not enough to degrade the magnetic spin significantly, which can make  $w_m$  be larger than  $w_1$  but smaller than  $w_2$ .

**Table. 2**Magnetic signal loss in non-scratched region with temperature. The magnetic phase angle (peak-to-peak amplitude) were estimated from the data in Fig. 6g.

Temperature	Magnetic phase angle (°) (pk to pk amplitude)	Percentage loss
Unheated	0.39	0%
100 °C	0.35	10.3%
300 °C	0.20	48.6%
400 °C	0.13	66.8%
500 °C	0.065	83.4%
600 °C	N/A	~ 100%

area exhibit a very clear contrast (i.e., the large magnetic phase angle amplitude) and shape of 2T patterns at room temperature. However, the amplitude became weak with increasing temperature, indicating the thermal degradation of magnetization. Fig. 6g shows the change in the magnetic signal strength with the temperature, and the magnetic signal loss is summarized in Table 2. At each temperature, the magnetic phase angle data were obtained along the red straight line between two red triangles in the MFM images. The peak-to-peak amplitude of the magnetic phase angle was about 0.39° for the unheated sample. When the PMR media sample was heated to 100 °C, the magnetic signal of the 2T patterns did not change noticeably, and its amplitude decreased by 10.3% compared to the unheated sample. This result is well explained by the MFM images of the unheated and 100 °C heated samples in Fig. 6a and b, respectively. However, when the sample was heated to the temperature higher than 300 °C, the magnetic signal was significantly reduced. Even though the contrast and shape of the 2T patterns were still well defined at 300 °C, the magnetic signal decreased by 48.6% in the signal amplitude. With the heat processed to 600 °C, the magnetic signal was almost lost. Accordingly, the 2T magnetic patterns in the MFM image were completely deteriorated, and thus the magnetic signal was not detectable at 600 °C by the MFM measurement. It is noted that when the PMR media sample is exposed to the controlled temperature, each magnetic grain in the magnetic layer may have different temperature responses. Some magnetic grains of magnetic recording thin film may have higher thermal instability than others due to the smaller volume (V) or lower magnetocrystalline anisotropy (K). Accordingly, these magnetic grains can trigger the thermal agitation (or superparamagnetism) of magnetic spins (moments) at a relatively lower temperature. This is called 'thermal degradation of magnetization' in this manuscript: the higher temperature, the more magnetic grains with thermal degradation. Therefore, considering the magnetization is obtained by  $M_s = \sum M_{si}$ , the 2T patterns' magnetic amplitude decreases with increasing temperature due to the thermal degradation of magnetization.

The influence of temperature on the magnetic properties in the scratched area was also investigated. The scratched areas in Fig. 6 were zoomed-in to better visualize the border of scratched and non-scratched areas, as shown in Fig. S5 (Supplementary Material). At each heat-processed condition, the MFM data (i.e., magnetic phase angle) were obtained at the same location along the red straight line crossing the scratch track, as illustrated in Figs. S5a - S5f (Supplementary Material). The results are plotted in Fig. 7. Examining the magnetic signals near the scratch center (xspan = 0.34  $\mu$ m) in Fig. 7a, the baseline amplitude and magnetic phase were lost completely due to the high local contact stress, i.e., the peak-to-peak amplitude was smaller than 0.1° without a sine waveform. These magnetic signals were permanently damaged and did not change during the heating process. However, the magnetic signals adjacent to the scratch track exhibited different responses to the temperature, as evidenced by the magnetic signals near the right wedge area (x-span = 0.48  $\mu$ m) of the scratch track in Fig. 7a. As discussed in Fig. 5, since the wedge area develops the relatively lower contact stress than the scratch center area, the magnetic signals are weakened without permanent damage. When the sample was heated to 100 °C - 300 °C (Fig. 7a, orange and yellow curves), the weakened magnetic signals near the right wedge area recovered dramatically, i.e., the peak-to-peak amplitude recovered to about 0.3° with a sine waveform. The thermalinduced realignment of magnetic spins can explain the magnetic recovery mechanism through the thermal excitations and energy equilibration process in magnetic domains. When the sample was further heated above 400 °C, the recovered magnetic signals near the right wedge area were degraded as shown in Fig. 7b, which could be caused by the higher thermal energy than the stress energy. It is noted that the left side of the scratch track developed the lower contact stress and, thus, the less magnetic damage due

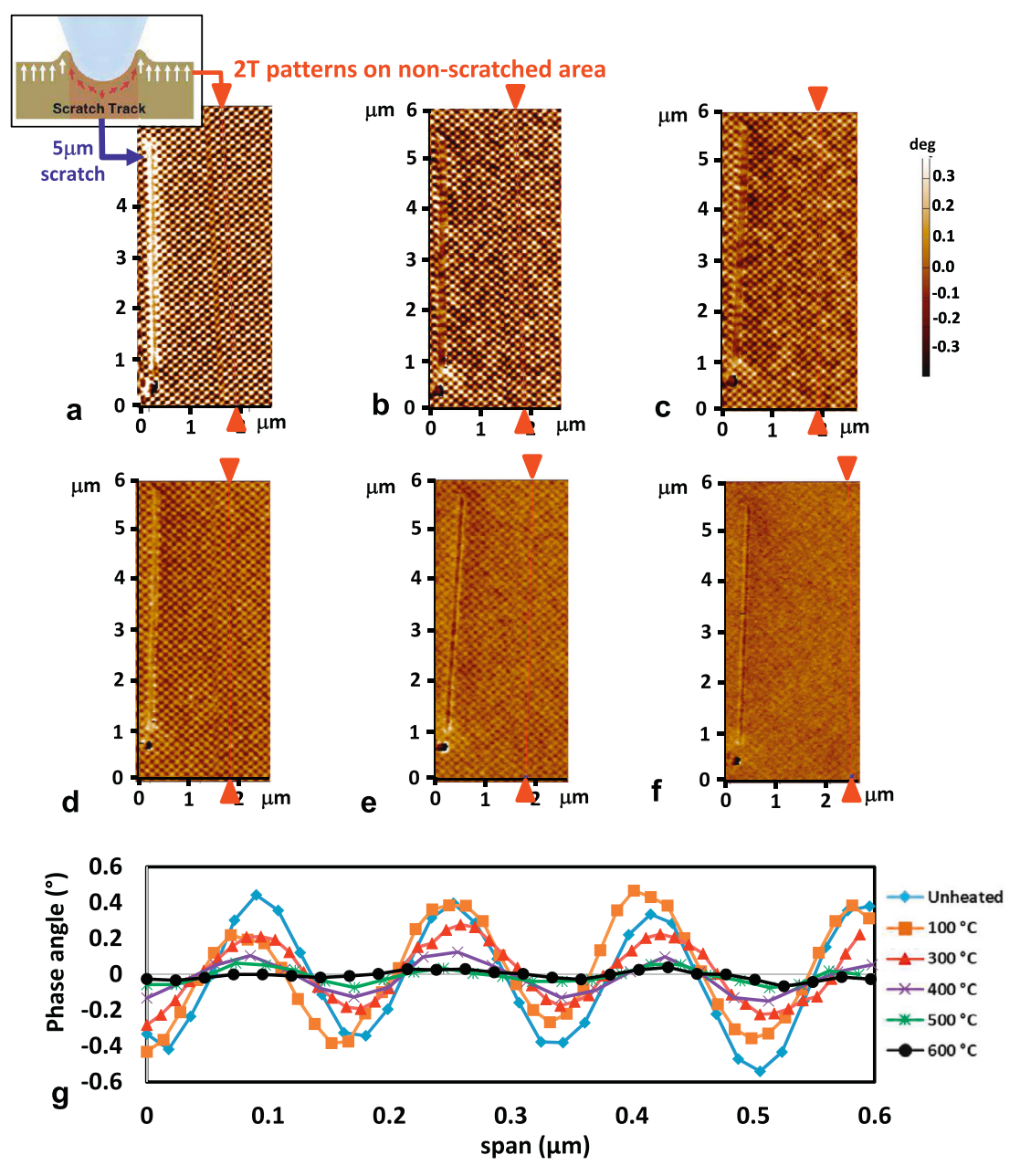


**Fig. 6.** Effect of temperature on magnetic domains and signals of PMR media. MFM measurements were performed on the media sample with 31.9 mN nanoscratch test. The MFM images were obtained after heating the sample to **a** room temperature (Unheated), **b** 100 °C, **c** 300 °C, **d** 400 °C, **e** 500 °C, and **f** 600 °C. **g** Change in magnetic phase angle along the 2T magnetic patterns in non-scratched region with temperature. At each temperature, the phase angle data were obtained along the red straight line between two red triangle in the MFM images. The non-scratched area shows clear 2T magnetic domains at room temperature, but they are tarnished with increasing temperature due to the weakened magnetic strength.

to the tip slating to the right during the nanoscratch experiment. Accordingly, the magnetic signals on the left wedge of the scratch in Fig. 7a showed similar responses to the applied heat as those of the non-scratched area.

# 3.5. Change in physical morphology of scratch with heat treatment

At each temperature, the scratch profile was investigated using AFM data. As shown in Fig. 8a, the 31.9 mN constant-load nanoscratch produced a scratch depth of 7.9  $\pm$  2.0 nm at room temperature. When the sample temperature increased to 300 °C, the scratch depth decreased significantly to about 1.4 nm. The reduction of scratch depth can be explained by the formation of metal oxides on the scratch surface. At the temperature of 400 °C and above, surprisingly the scratch became deeper again, as shown

in Fig. 8b. This unexpected scratch deepening process can be explained by a) the evaporation of platinum oxide at high temperature and b) the phase transition of Co-based magnetic materials from hexagonal close packed (HCP) to face centered cubic (FCC) structures by the combined effects of stress and temperature near the scratch center. The scratch recovery and deepening mechanisms are further discussed in Section 4.

### 4. Discussion

# 4.1. Scratch deepening by evaporation of metal oxides

During the nanoscratch experiment, the magnetic layer beneath the DLC coating is exposed to the air, forming metal oxides on the scratch surface. The magnetic layer of the tested PMR media

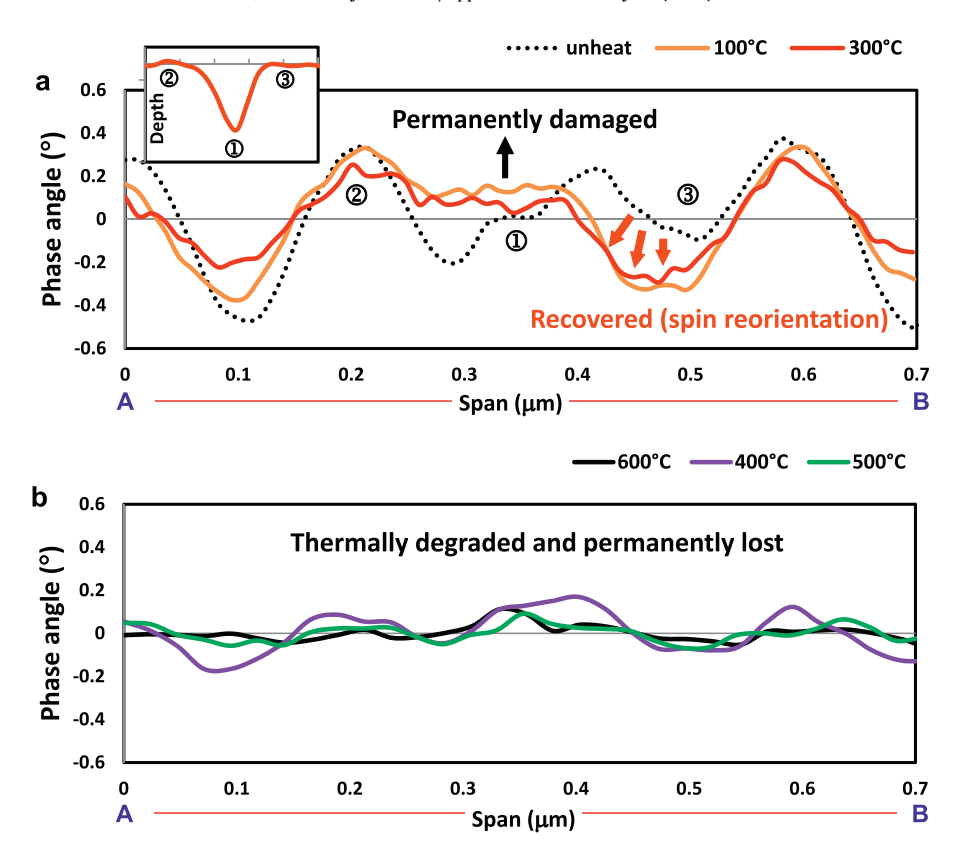


Fig. 7. Change in magnetic phase angle at the contact stressed area with temperature. a Magnetic phase angles at the temperatures up to 300 °C. Magnetic signals near the scratch center (the high stressed zone, ①) were permanently damaged, whereas the lightly stressed zone at the right wedge side (③) showed significant recovery of magnetic signals by the applied heat. The inlet is the actual scratch profile from the constant load nanoscratch with 31.9 mN at unheated condition. b Magnetic phase angles at the temperature of 400 °C ~ 600 °C. Most of magnetic signals were thermally degraded at the escalated temperature. The MFM data were obtained along the red straight line between points A to B crossing the scratch track in supplementary Fig. 2.

is oxidized to CoO, Cr<sub>2</sub>O<sub>3</sub>, and PtO<sub>2</sub> on the scratched area at elevated temperatures. These metal oxides grow with increasing temperature [33-35], filling up the scratch valley as schematically described in Fig. 9a and b. However, it is known that platinum oxide  $(PtO_2)$  on heating in the air starts to evaporate at 400 °C – 500 °C [35]. Due to the increasing vapor pressure at the higher temperature, the volatile PtO2 changes into the gaseous phase, thereby being emitted from the scratched surface as shown in Fig. 9c [36–38]. At the escalated temperatures up to 600 °C, the scratch deepens due to the further evaporation of PtO2, as shown in Fig. 9d. HAMR technology (as a potential candidate to make a breakthrough of data storage capacity in the HDD industry) uses a thermal excitation of magnetic thin films at about 500 °C to lower the coercivity, and it also increases the probability of HDI contacts, resulting in scratch damages on the media surfaces. Therefore, this discovery of a scratch deepening mechanism can contribute to designing future HAMR media to secure HDD's long-term reliability.

# 4.2. Change in mechanical property of PMR media after heat treatment

The hardness of unheated and 600 °C heated PMR media samples was measured using the nanoindentation technique. Fig. 10 provides the resulting hardness values with respect to the contact depth. When the nanoindentation experiment is performed on a multilayered sample, the measured hardness at a higher contact depth reflects the mechanical properties of underlying layers and substrate [39–41]. Since we are interested in the hardness of the magnetic layer (CoCrPt  $+ \alpha$ ) of PMR media in Fig. 1a, we mostly focused on the measured hardness values at a shallow contact depth  $+ \alpha$ 0 of Fig. 10, it is found that the hardness of the

600 °C heated sample ( $H_{\rm heated} = \sim 12.3$  GPa) was lower than that of the unheated sample ( $H_{\rm unheated} = \sim 13.3$  GPa) at the shallow contact depth. For cobalt or cobalt-rich compounds with HCP structure, it is known that their crystal structure transforms into a FCC structure at a temperature of 400 °C – 500 °C [42–44]. It is also reported that HCP cobalt has higher yield strength and stiffness than FCC cobalt [45,46]. Considering that the 600 °C heated PMR media had a lower hardness in Fig. 10, it is suggested that the magnetic layer has experienced the heat-induced phase (structure) transformation, and thus its structure becomes a mixture of HCP and FCC phases. This phase transformation of the PMR media can explain the thermal degradation of magnetic properties and the scratch deepening phenomenon at the high temperature in Fig. 8b. The crystal structure of PMR media related to stress and temperature is further discussed in the following Section 4.3.

# 4.3. Thermo-magneto-mechanical material behavior

Cobalt undergoes a phase transition from HCP to FCC when compressive stress or heat is applied. Non-hydrostatic compressive stress induces a phase transition from a low-pressure magnetic HCP structure to a high-pressure nonmagnetic FCC through the mixture of HCP-FCC [47]. Torchio et al. [48] have reported that when HCP and FCC phases coexist under non-hydrostatic compression, its ferromagnetism disappears. The ionic lattice vibration mainly causes a phase change from a low-temperature ferromagnetic HCP to a high-temperature nonmagnetic FCC around 700 K [49].

In this study, the nanoscratch experiment produces compressive and shear stresses in the magnetic layer of PMR media. Notably, the magnetic grains beneath the scratch center experience high

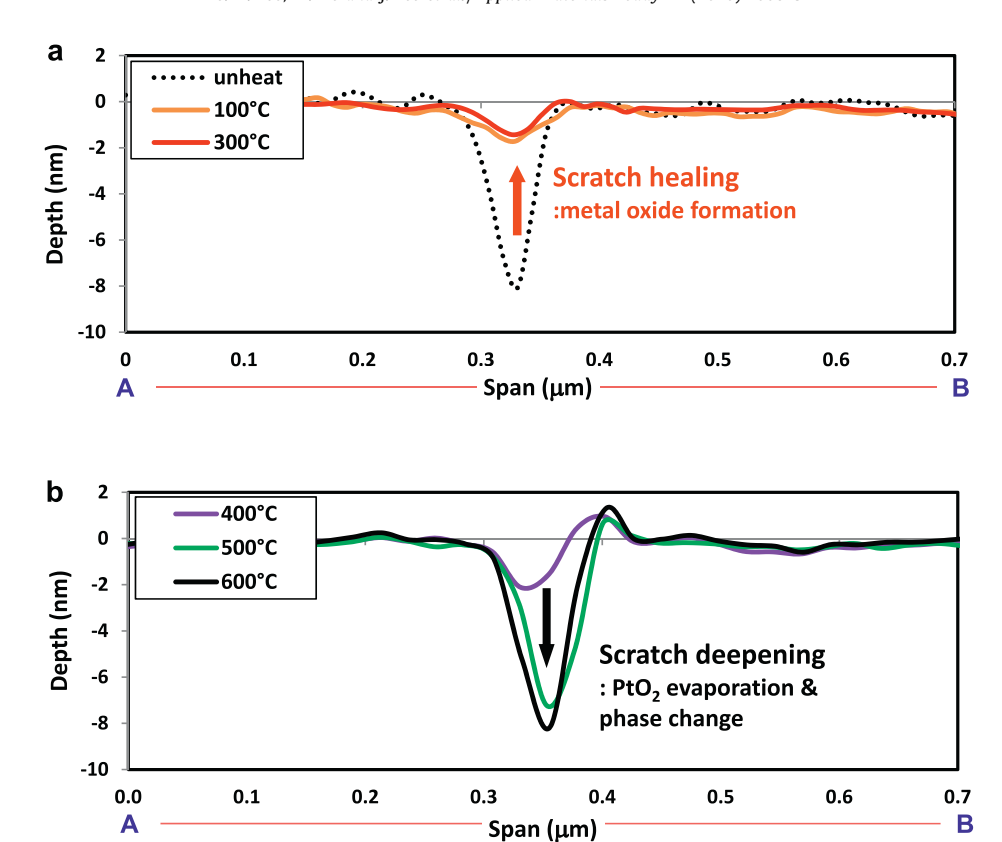


**Fig. 8.** Variations of physical morphology of scratch with temperature. **a** AFM topographical scratch profile at room temperature ~ 300 °C. The scratch was recovered by the formation of metal oxides. **b** and (b) AFM topographical scratch profile at 400 °C ~ 600 °C. The AFM data were obtained along the red straight line from A to B crossing the scratch track in supplementary Fig. 2.

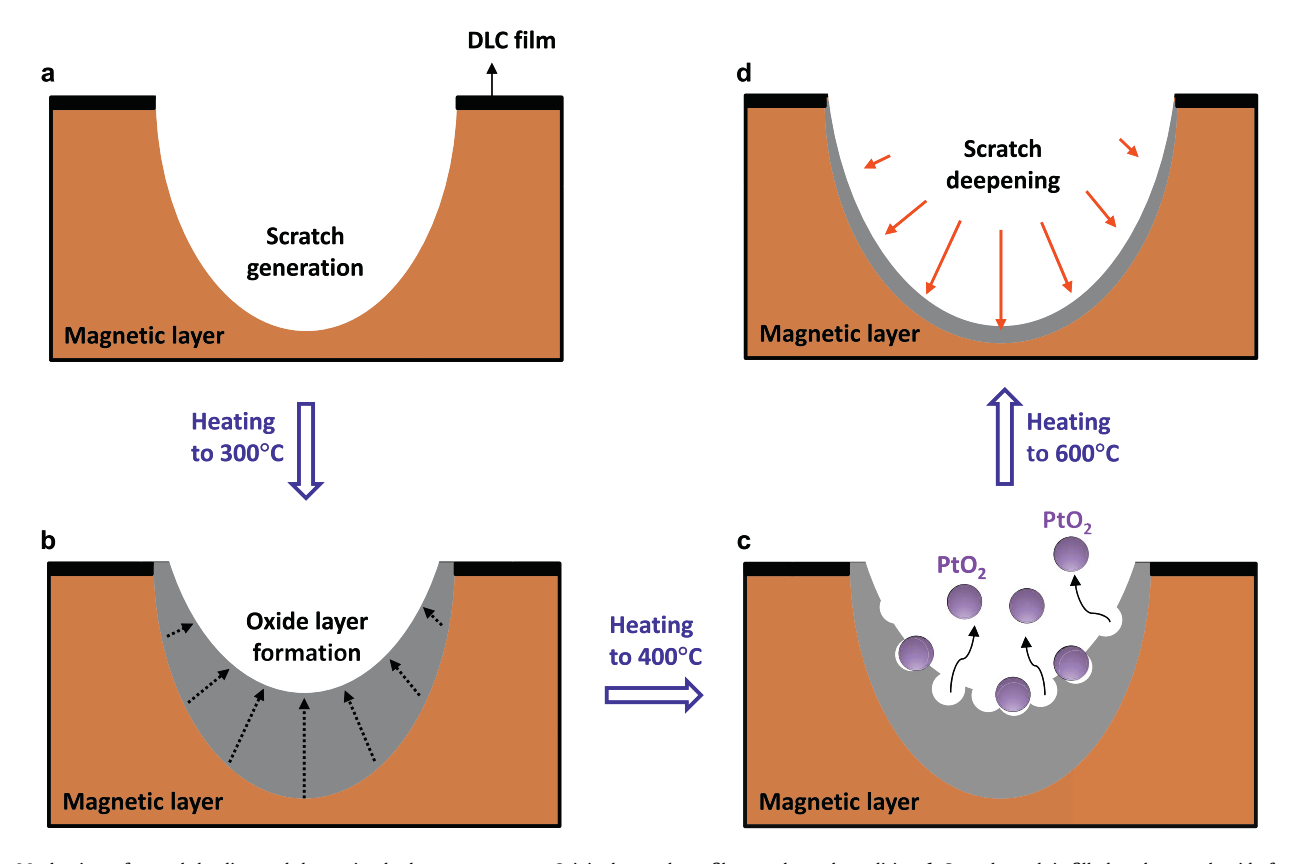
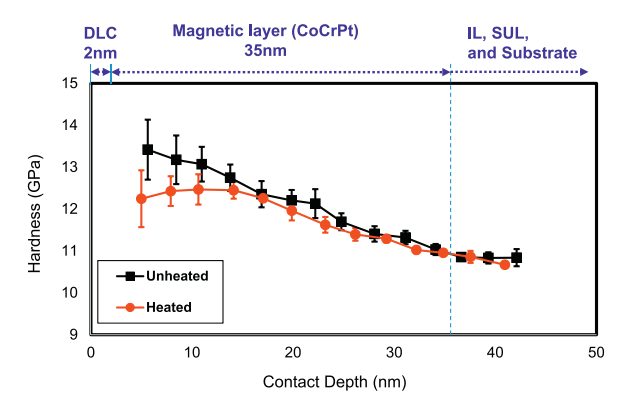


Fig. 9. Mechanism of scratch healing and deepening by heat treatment. a Original scratch profile at unheated condition. b Scratch track is filled up by metal oxide formation when the temperature increased up to 300 °C. c Evaporation of platinum oxide (PtO<sub>2</sub>) initiates the deepening process of scratch at 400 °C. d The scratch is further deepened by the continuous evaporation of PtO<sub>2</sub> at 600 °C.



**Fig. 10.** Comparison of measured hardness between unheated and  $600\,^{\circ}\text{C}$  heated PMR media with respect to the contact depth. The hardness of CoCrPt magnetic layer of the  $600\,^{\circ}\text{C}$  heated sample is lower than that of the unheated sample.

compressive stress which is the source for the HCP-to-FCC phase transition and decreases the c/a ratio of HCP crystal [48]. Accordingly, the unheated scratched sample showed the permanent damage of magnetic signals at the scratch center (area ① in Figs. 2b and 7a). This is attributed to the stress-induced phase transformation from HCP to HCP-FCC mixture. For the area outside the scratch track (area ③ in Figs. 2b and 7a), the magnetic layer retained the ferromagnetic HCP phase due to the relatively low contact stress. When the temperature increased up to 300 °C, the magnetic signals showed significant recovery. This confirms that the magnetic grains outside the scratch track are still in the ferromagnetic HCP phase, enabling the magnetic signal recovery by the heat treatment. However, when the temperature increased to 400 °C and above, no further improvement of magnetic signals was found, indicating that the ferromagnetism disappeared.

The scratch deepening with the heat treatment in Fig. 8b can also be explained by the phase transition of PMR media caused by stress and temperature. During the nanoscratch, HCP and FCC crystal structures coexist near the scratch center due to the high non-hydrostatic compressive stress. The HCP-FCC mixed phase has a lower transition temperature to the FCC phase than the unstressed HCP structure outside the scratch [47,48]. Therefore, when the temperature increases to 400 °C and above, the HCP-FCC mixed grains underneath the scratch center become a single FCC phase, resulting in the reduction of grain height, thus deepening the scratch, whereas the grains outside the scratch retain their HCP or HCP-FCC mixed structure.

### 5. Conclusions

The magnetic and morphological responses of the ferromagnetic thin film of the magnetic recording media to the stress and temperature were investigated. The 2T-patterned magnetic domains in the unscratched area were gradually destroyed with increasing temperature due to the thermal agitation of magnetic spins, and the magnetic signals disappeared completely at 600 °C. On the other hand, the magnetic domains in the scratched area exhibited a different response to temperature. The high local stress permanently damaged the magnetic signals at the scratch center so that the magnetic signals were not recovered by the heat treatment. Interestingly, the magnetic signals adjacent to the scratch center were initially damaged by stress but were significantly recovered when heated to 300 °C retaining the ferromagnetism. The combined stress-temperature helps with the reorientation of magnetic spins to be aligned with each other. The scratch healing and deepening behaviors of the magnetic layer were observed in response to temperature. When the nanoscratched PMR media was heated to 300 °C, the scratch depth decreased from 7.9 nm to 1.4 nm due to the formation of metal oxides, such as CoO,  $\rm Cr_2O_3$ , and  $\rm PtO_2$ . It is discovered that the scratch deepened above 400 °C, as  $\rm PtO_2$  evaporates and the phase changed to FCC from HCP. The research outcomes in this study help design robust and reliable magnetic devices, including HDD, magnetic sensors, and actuators operated under combined stress and thermal condition.

#### 6. Author contributions

C.-D. Yeo and Y.-K. Hong designed the project and supervised the research activities. M. He, J. Lee, and N. Shah conducted the experiments including TEM, nanoscratch, AFM and MFM. Y.-K. Hong, J.H. You, and M. Choi analyzed the magnetic signal data from MFM and nanoscratch results. D. Purani prepared and magnetized the PMR media sample having a customized 2T magnetic patterns. J.K. Lee performed nanoindentation experiment. All authors wrote and reviewed the manuscript.

# 7. Data availability

Experimental data and numerical simulation code from this study are available from Dr. Chang-Dong Yeo (email: chang-dong.yeo@ttu.edu) upon reasonable request.

### **Declaration of Competing Interest**

The authors declare that they have no known competing financial interests or personal relationships that could have appeared to influence the work reported in this paper.

### Acknowledgment

This work was, supported by the NSF-CMMI under award numbers 1463078 and 1463301, the NSF under award number IIP 1650564, and Seagate Technology under the agreement number 96723.0.

### Supplementary materials

Supplementary material associated with this article can be found, in the online version, at doi:10.1016/j.apmt.2020.100825.

# Appendix: Surface sliding contact model

The von Mises stress contour on the PMR media during the nanoscratch experiment (Fig. 2b) was obtained from the Hamilton's sliding contact solution [50], where the semi-contact width (a) was calculated by the Hertzian solution [51], i.e.,  $a=(3PR/4E^*)^{1/3}$ .  $E^*$  is the reduced elastic modulus given by  $1/E^*=(1-\nu_d{}^2)/E_d+(1-\nu_i{}^2)/E_i$ , where the subscripts i= indenter (or scratch tip) and d= PMR media. Table S1 (Supplementary Material) summarizes the material properties and geometrical parameters used for the numerical simulation of contact stress [52]. First, the surface stress components within the contact area ( $r \le a$ ;  $r=[x^2+y^2]^{1/2}$ ) are calculated by

$$\begin{split} \sigma_{x} &= \frac{3P}{2\pi a^{3}} \left[ \frac{1}{r^{2}} \left\{ \frac{y^{2} - x^{2}}{r^{2}} \left( \frac{1 - 2\nu}{3} \left\{ \left( a^{2} - r^{2} \right)^{\frac{3}{2}} - a^{3} \right\} \right) - \left( x^{2} + 2\nu y^{2} \right) \left( a^{2} - r^{2} \right)^{\frac{1}{2}} \right\} \right] \\ &+ \frac{3Q}{2\pi a^{3}} \left[ -\frac{\pi x}{2} \left( \frac{\nu}{4} + 1 \right) \right]. \end{split} \tag{1}$$

$$\begin{split} \sigma_y &= \frac{3P}{2\pi a^3} \bigg[ \frac{1}{r^2} \bigg\{ \frac{x^2 - y^2}{r^2} \left( \frac{1 - 2\nu}{3} \left\{ \left( a^2 - r^2 \right)^{\frac{3}{2}} - a^3 \right\} \right) - \left( y^2 + 2\nu x^2 \right) \left( a^2 - r^2 \right)^{\frac{1}{2}} \bigg\} \bigg] \\ &+ \frac{3Q}{2\pi a^3} \bigg[ - \frac{3\pi \nu x}{2} \bigg], \end{split}$$

(2)

$$\sigma_z = -\frac{3P}{2\pi a^3} (a^2 - r^2)^{1/2},\tag{3}$$

$$\tau_{xy} = \frac{3P}{2\pi a^3} \left[ \frac{xy(1-2\nu)}{r^4} \left\{ \left(a^2 - r^2\right)^{1/2} \left( -r^2 - \frac{2}{3} \left(a^2 - r^2\right) \right) + \frac{2}{3} a^3 \right\} \right]$$

$$+\frac{3Q}{2\pi a^3} \left[ \frac{\pi \nu}{4} \left( \frac{\nu}{2} - 1 \right) \right],\tag{4}$$

$$\tau_{yz} = 0, (5)$$

$$\tau_{zx} = \frac{3Q}{2\pi a^3} \left[ -\left(a^2 - r^2\right)^{1/2} \right],\tag{6}$$

Second, the surface stress components outside the contact area (r > a) are obtained by

$$\sigma_{x} = \frac{3P}{2\pi a^{3}} \left[ \frac{(1-2\nu)(x^{2}-y^{2})a^{3}}{3r^{4}} \right] + \frac{3Q}{2\pi a^{3}} \left[ -x\left(1+\frac{\nu}{4}\right)\varphi + \frac{axM_{0}}{r^{4}} \left\{ -\nu M_{0}^{2} \left(\frac{3}{2} - \frac{2x^{2}}{r^{2}}\right) + \frac{7\nu r^{2}}{4} - 2\nu x^{2} + r^{2} \right\} \right],$$

$$(7)$$

$$\sigma_{y} = \frac{3P}{2\pi a^{3}} \left[ \frac{(1-2\nu)(y^{2}-x^{2})a^{3}}{3r^{4}} \right] + \frac{3Q}{2\pi a^{3}} \left[ -\frac{3}{4}x\varphi + \frac{axM_{0}}{r^{4}} \left\{ \nu a \left( \frac{1}{2} - \frac{2y^{2}}{r^{2}} \right) + \frac{3\nu r^{2}}{4} \right\} \right], \quad (8)$$

$$\tau_{xy} = \frac{3P}{2\pi a^{3}} \left[ \frac{2a^{2}xy(1-2\nu)}{3r^{4}} + \frac{3Q}{2\pi a^{3}} \left[ \frac{y}{2} \left( \frac{\nu}{2} - 1 \right) \varphi \right] \right]$$

$$+ \frac{ayM_0}{r^4} \left\{ -\nu M_0 \left( \frac{1}{2} - \frac{2x^2}{r^2} \right) + \frac{\nu r^2}{4} - 2\nu x^2 + \frac{r^2}{2} \right\} \right] \right], \quad (9)$$

$$\sigma_{z} = \tau_{yz} = \tau_{zx} = 0, \tag{10}$$

where  $M_0 = (r^2 - a^2)^{1/2}$  and  $\phi = \tan^{-1}(a^2 - r^2)^{1/2}$ .

To deliver explicit explanation of material degradation of PMR media during nanoscratch experiment, the surface contact stresses are mapped using the von Mises stress ( $\sigma_v$ ):

$$\sigma_{\nu} = \sqrt{\frac{1}{2} \left\{ (\sigma_{x} - \sigma_{y})^{2} + (\sigma_{y} - \sigma_{z})^{2} + (\sigma_{z} - \sigma_{x})^{2} + 6 \left( \tau_{xy}^{2} + \tau_{yz}^{2} + \tau_{zx}^{2} \right) \right\}},$$
(11)

### References

- [1] Seagate Technology, The story of global data storage, https://www.seagate.com/our-story/data-age-2025/, 2020 (accessed 1 July 2020).
- [2] W. Daeng-am, P. Chureemart, R. Chantrell, J. Chureemart, Granular micromagnetic model for perpendicular recording media: quasi- static properties and media characterization, J. Phys. D: Appl. Phys. 52 (2019) 425002, doi:10.1088/1361-6463/ab33d6.
- [3] D. Weller, O. Mosendz, G. Parker, S. Pisana, S.T. Santos, L10 FeP tX-Y media for heat-assisted magnetic recording, Phys. Status Solidi A 210 (2013) 1245–1260, doi:10.1002/pssa.201329106.
- [4] D. Weller, G. Parker, O. Mosendz, E. Champion, B. Stipe, X. Wang, T. Klemmer, G. Ju, A. Ajan, A HAMR Media Technology Roadmap to an Areal Density of 4Tb/in2, IEEE Trans. Magn. 50 (2013) 3100108, doi:10.1109/TMAG.2013.2281027
- [5] B. Marchon, T. Pitchford, Y.-.T. Hsia, S. Gangopadhyay, The Head-Disk Interface Roadmap to an Areal Density of 4 Tbit/in2, Advances in Tribology (2013) 521086, doi:10.1155/2013/521086.
- [6] S. Iwasaki, Perpendicular magnetic recording Evolution and future, IEEE Trans. Magn. 20 (1984) 657–662, doi:10.1109/TMAG.1984.1063563.
- [7] I. Tudosa, C. Stamm, A.B. Kashuba, F. King, H.C. Siegmann, J. Stöhr, G. Ju, B. Lu, D. Weller, The ultimate speed of magnetic switching in granular recording media, Nature 428 (2004) 831–833, doi:10.1038/nature02438.
- [8] B. Lu, D. Weller, A. Sunder, G. Ju, X. Wu, High anisotropy CoCrPt(B) media for perpendicular magnetic recording, J. Appl. Phys. 93 (2003) 6751–6753, doi:10. 1063/1.1557715.

- [9] Q. Dai, U. Nayak, D. Margulies, B. Marchon, R. Waltman, K. Takano, J. Wang, Tribological issues in perpendicular recording media, Tribol. Lett 26 (2007) 1– 9, doi:10.1007/s11249-006-9174-9.
- [10] A. Suh, A.A. Polycarpou, Adhesive contact modeling for sub-5-nm ultralow flying magnetic storage head-disk interfaces including roughness effects, J. Appl. Phys. 97 (2005) 104328, doi:10.1063/1.1914951.
- [11] F.E. Talke, On tribological problems in magnetic disk recording technology, Wear 190 (1995) 232–238, doi:10.1016/0043-1648(95)06730-2.
- [12] K. Komvopoulos, Head-disk interface contact mechanics for ultrahigh density magnetic recording, Wear 238 (2000) 1-11, doi:10.1016/S0043-1648(99) 00333-6.
- [13] M. Kryder, E. Gage, T. McDaniel, W. Challener, R. Rottmayer, G. Ju, Y.-T. Hsia, M. Erden, Heat assisted magnetic recording, Proceedings of the IEEE 96 (2008) 1810–1835, doi:10.1109/IPROC.2008.2004315.
- [14] J. Matlak, E. Rismaniyazdi, K. Komvopoulos, Nanostructure, structural stability, and diffusion characteristics of layered coatings for heat-assisted magnetic recording head media, Sci. Rep. 8 (2018) 9807, doi:10.1038/ s41598-018-77688-4
- [15] R.E. Rottmayer, et al., Heat-assisted magnetic recording, IEEE Trans. Magn 42 (2006) 2417–2421, doi:10.1109/TMAG.2006.879572.
- [16] G. Ju, et al., High density heat-assisted magnetic recording media and advanced characterization-progress and challenges, IEEE Trans. Magn. 51 (2015) 3201709. doi:10.1109/TMAG.2015.2439690
- [17] J. Zhu, X. Zhu, Y. Tang, Microwave assisted magnetic recording, IEEE Trans. Magn 44 (2007) 125–131, doi:10.1109/TMAG.2007.911031.
- [18] L. Pan, D.B. Bogy, Heat-assisted magnetic recording, Nat. Photonics 3 (2009) 189–190, doi:10.1038/nphoton.2009.40.
- [19] W.A. Challener, et al., Heat-assisted magnetic recording by a near-field transducer with efficient optical energy transfer, Nat. Photonics 3 (2009) 220–224, doi:10.1038/nphoton.2009.26.
- [20] J. Park, Y.-.K. Hong, S.-.G. Kim, L. Gao, J.-.U. Thiele, Magnetic properties of Fe-Mn-Pt for heat assistant magnetic recording applications, J. Appl. Phys. 117 (2015) 053911, doi:10.1063/1.4907570.
- [21] J. Park, Y.-.K. Hong, C.-.D. Yeo, S.-.G. Kim, D. Kuo, L. Gao, J.-.U. Thiele, Electronic structure and magnetic properties of Mn substituted Fe-Pt, IEEE Trans. Magn. 52 (2016) 3201904, doi:10.1109/TMAG.2015.2511757.
- [22] J. Ye, et al., . Determination of magnetic anisotropy constants in Fe ultrathin film on vicinal Si(111) by anisotropic magnetoresistance, Sci. Rep. 3 (2013) 2148, doi:10.1038/srep02148.
- [23] H. Wang, C. Du, P.C. Hammel, F. Yang, Strain-tunable magnetocrystalline anisotropy in epitaxial Y3Fe5O12 thin films, Phys. Rev. B 89 (2014) 134404, doi:10.1103/PhysRevB.89.134404.
- [24] Y. Yan, et al., Correlation between tunability and anisotropy in magnetoelectric voltage tunable inductor (VTI), Sci. Rep. 7 (2017) 16008, doi:10.1038/ s41598-017-14455-0.
- [25] M.-.Y. Im, J.--R. Jeong, S.-.C. Shin, Saturation magnetostriction coefficient measurement of CoCrPt alloy thin films using a highly sensitive optical deflection-detecting system, J. Appl. Phys. 97 (2005) 10N110, doi:10.1063/1.1850853.
- [26] O. Ciubotariu, et al., . Strain-induced perpendicular magnetic anisotropy and Gilbert damping of Tm3Fe5O12 thin films, Sci. Rep. 9 (2019) 17474, doi:10.
- [27] W.C. Oliver, G.M. Pharr, An improved technique for determining hardness and elastic modulus using load and displacement sensing indentation experiments, J. Mater. Res. 7 (1992) 1564–1583, doi:10.1557/JMR.1992.1564.
- [28] C.-D. Yeo, A.A. Polycarpou, J.D. Kiely, Y.-T. Hsia, Nanomechanical properties of ultra-thin carbon film overcoats using the nanoindentation technique, J. Mate. Res. 22 (2007) 141–151, doi:10.1557/jmr.2007.0007.
- [29] M. Furukawa, J. Xu, Y. Shimizu, Y. Kato, Mechanism study of scratch-induced demagnetization for perpendicular magnetic disks, Microsyst. Technol 16 (2010) 221–226, doi:10.1007/s00542-009-0831-4.
- [30] S. Lee, M. He, G. Abo, Y.-.K. Hong, C.-.D. Yeo, Effects of mechanical contact stress on magnetic properties of ferromagnetic film, J. Appl. Phys. 112 (2012) 084901, doi:10.1063/1.4759330.
- [31] S.-C. Lee, et al., Stress induced permanent magnetic signal degradation of perpendicular magnetic recording system, J. Tribol. 131 (2009) 011904, doi:10. 1115/1.2991123.
- [32] M. Furukawa, J. Xu, Y. Shimizu, Y. Kato, Scratch-Induced Demagnetization of Perpendicular Magnetic Disk, IEEE Trans. Magn 44 (2008) 3633–3636, doi:10. 1109/TMAG.2008.2001593.
- [33] H.G. Tompkins, J.A. Augis, The oxidation of cobalt in air from room temperature to 467°C, Oxidat. Metal. 16 (1981) 355–369, doi:10.1007/BF00611349.
- [34] G. Thurner, P. Holloway, Oxidation of Polycrystalline Chromium between 30°C and 400°C, Acta Physica Polonica A 81 (1992) 273–283 10.12693%2FA-PhysPolA.81.273.
- [35] J.C. Chaston, The Oxidation of the Platinum Metals, Platinum Metals Rev. 19 (1975) 135–140.
- [36] C. Carrillo, et al., Regenerative trapping: how Pd improves the durability of Pt diesel oxidation catalysts, Appl. Catal. B 218 (2017) 581–590, doi:10.1016/j. apcatb.2017.06.085.
- [37] P.N. Plessow, F. Abild-Pedersen, Sintering of Pt nanoparticles via volatile PtO2: simulation and comparison with experiments, ACS Catal. 6 (2016) 7098–7108, doi:10.1021/acscatal.6b01646.
- [38] T.R. Johns, et al., Relating adatom emission to improved durability of Pt-Pd diesel oxidation catalysts, J. Catal. 328 (2015) 151-164, doi:10.1016/j.jcat.2015. 03.016.

- [39] K.M. Lee, C.-.D. Yeo, A.A. Polycarpou, Mechanical property measurements of thin-film carbon overcoat on recording media towards 1Tbit/in2, J. Appl. Phys. 99 (2006) 08G906, doi:10.1063/1.2166595.
- [40] Z. Xu, D. Rowcliffe, Finite element analysis of substrate effects on indentation behaviour of thin films, Thin Solid Films 447–448 (2004) 399–405, doi:10.1016/S0040-6090(03)01071-X.
- [41] H. Buckle, The Science of Hardness Testing and Its Research Applications, American Society for Metals, Metals Park, OH, 1973.
- [42] E.A. Owen, D. Jones, Effect of grain size on the crystal structure of cobalt, Proc. Phys. Soc. B 67 (1954) 456-466, doi:10.1088/0370-1301/67/6/302.
- [43] W. Bollmann, On the phase transformation of cobalt, Acta Metall 9 (1961) 972.
- [44] V. O'Shea, P. Piscina, N. Homs, G. Aromí, J. Fierro, Development of hexagonal closed-packed cobalt nanoparticles stable at high temperature, Chem. Mater
- 21 (2009) 5637–5643, doi:10.1021/cm900845h.
  [45] A. Mani, A. Salinas-Rodriguez, H.F. Lopez, Deformation induced FCC to HCP transformation in a Co-27Cr-5Mo-0.05C alloy, Mat. Sci. Eng. A 528 (2011) 3037-3043, doi:10.1016/j.msea.2010.12.024.
- [46] X. Li, D.L. Irving, L. Vitos, First-principles investigation of the micromechanical properties of fcc-hcp polymorphic high-entropy alloys, Sci. Rep. 8 (2018) 11196, doi:10.1038/s41598-018-29588-z.
- [47] C.S. Yoo, H. Cynn, P. Söderlind, V. Iota, New  $\beta$ (fcc)-Cobalt to 210GPa, Phys. Rev. Lett. 84 (2000) 4132, doi:10.1103/PhysRevLett.84.4132.
- [48] R. Torchio, et al., Structure and magnetism of cobalt at high pressure and low temperature, Phys. Rev. B 94 (2016) 024429, doi:10.1103/PhysRevB.94.024429.
- [49] R. Lizárraga, et al., First principles theory of the hcp-fcc phase transition in cobalt, Sci. Rep. 7 (2017) 3778, doi:10.1038/s41598-017-03877-5.
- [50] G.M. Hamilton, Explicit equations for the stresses beneath a sliding spherical contact, Proc Instn. Mech. Engrs 197C (1983) 53-59, doi:10.1243/PIME\_PROC\_ 1983 197 076 02.
- [51] K.L. Johnson, Contact Mechanics, Cambridge university press, Cambridge, 1985.
   [52] S. Lee, C.-D. Yeo, Microwear mechanism of head carbon film during head disk interface sliding contact, Tribol. Int 45 (2012) 30-37, doi:10.1016/j.triboint.2011.